Applied Catalysis B: Environmental 257 (2019) 117897

Contents lists available at ScienceDirect

Applied Catalysis B: Environmental

journal homepage: www.elsevier.com/locate/apcatb

Robust and efficient photocatalytic hydrogen generation of ReS_2/CdS and mechanistic study by on-line mass spectrometry and *in situ* infrared spectroscopy

Liqun Ye[a,*], Zhaoyu Ma[b], Yu Deng[a], Yinghao Ye[c], Li Wang[b], Mingpu Kou[b], Haiquan Xie[b], Zhikun Xu[d], Ying Zhou[c], Dehua Xia[e], Po Keung Wong[f]

[a] College of Materials and Chemical Engineering, Key Laboratory of Inorganic Nonmetallic Crystalline and Energy Conversion Materials, China Three Gorges University, Yichang, 443002, PR China
[b] Engineering Technology Research Center of Henan Province for Solar Catalysis, College of Chemistry and Pharmaceutical Engineering, Nanyang Normal University, Nanyang, 473061, PR China
[c] State Key Laboratory of Oil and Gas Reservoir Geology and Exploitation, School of Materials Science and Engineering, Southwest Petroleum University, Chengdu, 610500, PR China
[d] Key Laboratory for Photonic and Electric Bandgap Materials, Ministry of Education, Harbin Normal University, Harbin, 150025, PR China
[e] School of Environmental Science and Technology, Sun Yat-sen University, Guangzhou, 510275, PR China
[f] School of Life Sciences, The Chinese University of Hong Kong, Shatin, NT, Hong Kong SAR, PR China

ARTICLE INFO

Keywords:
rhenium sulfide
Cadmium sulfide
Hydrogen
Photocatalysis
Co-catalyst

ABSTRACT

Photocatalytic hydrogen evolution is an attractive technology to address the increasing energy crisis. The development of advanced photocatalysts presents an attractive but challenging issue. For the first time, we anchored inorganic ReS_2 via a facial hydrothermal route as co-catalyst to CdS nanorods for highly efficient H_2 evolution. CdS/ReS_2 composite photocatalyst containing 1 wt% of ReS_2 co-catalyst exhibits the highest photocatalytic H_2 evolution rates of 24.36 and 137.5 mmol h^{-1} g^{-1} using Na_2S-Na_2SO_3 and lactic acid as sacrificial reagents, respectively, corresponding to 127 and 8.8 fold enhancements, respectively, compared with bare CdS. The photocatalytic enhancement mechanism was elucidated by experimental means and theoretical calculations. The source of hydrogen and the fate of the sacrifice reagents were studied by *in situ* Fourier transform infrared (FT-IR) spectroscopy and on-line mass spectrometry. Our results showed that ReS_2 is a promising co-catalyst to achieve high photocatalytic hydrogen production from water under visible light irradiation.

1. Introduction

Energy shortage has become one of the most significant challenges in modern human society. Hydrogen obtained by photocatalytic water splitting induced by solar energy presents an alternative, renewable, and green energy, which plays a vital role in addressing the energy crisis [1,2]. To date, a variety of photocatalysts have been typically studied for hydrogen evolution [3–6]. Among them, one-dimensional (1D) CdS is a significant material for photocatalytic H_2 evolution due to its excellent optical properties and electronic structure [7]. Development of efficient strategies to further improve the H_2 production of CdS is crucial for practical applications. To this goal, various effective approaches such as element doping, construction of heterojunctions, or use of co-catalysts have been developed [8–10].

Recently, co-catalyst loading has attracted considerable attention due to its indispensable role in extracting photo-generated charge carriers, providing active sites for H^+ reduction and decreasing reaction energy barriers to promote photocatalytic H_2 generation [11,12]. However, most of the co-catalysts for hydrogen production are noble metals (Ag, Au, Pt, Pd, and Ru) [13–17]. To extend the family of co-catalysts, other non-metal-free materials, such as nickel-based co-catalysts (Ni, NiS_x, NiO_x, and Ni_2P), have been studied [18–22]. Unfortunately, these co-catalysts exhibit lower efficiencies and stabilities. Therefore, studies on advanced co-catalysts are highly desirable.

2D transition metal dichalcogenides (TMDs) such as MoS_2 and WS_2, with large interlayer spaces and weak van der Waals interactions between the layers, have been extensively investigated as efficient co-catalysts for hydrogen evolution [23,24]. Rhenium disulfide (ReS_2), a new kind of TMD, possesses extraordinary photocatalytic properties and has recently been explored as a promising photocatalyst for

* Corresponding author.
E-mail address: yeliquny@163.com (L. Ye).

https://doi.org/10.1016/j.apcatb.2019.117897
Received 8 March 2019; Received in revised form 15 May 2019; Accepted 22 June 2019
Available online 05 July 2019

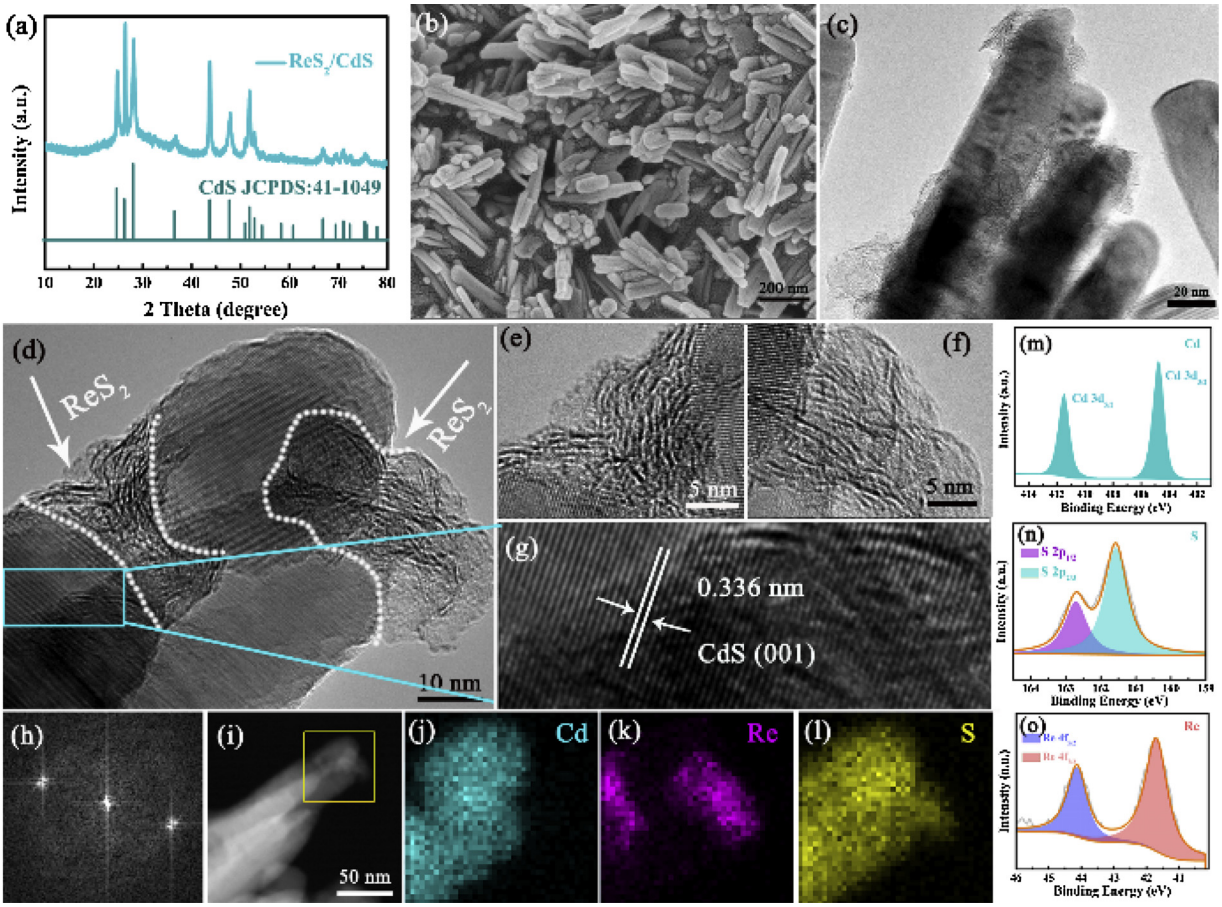

Fig. 1. Composition and morphological characterizations of ReS_2/CdS. (a) XRD pattern, (b) SEM image, (c, d) TEM and (e–g) HRTEM images, (h) corresponding FFT pattern of d, (i–l) STEM image, (i–l) EDS elemental mapping, and (m–o) XPS analysis of ReS_2/CdS.

hydrogen evolution due to its remarkable electron–hole separation [25–29]. For example, *Fu* et al. reported the highest photocatalytic hydrogen evolution efficiency for ReS_2 nanowalls prepared via two-electron catalytic reaction among TMD composite photocatalysts [25]. ReS_2 is an emerging material and a promising candidate to replace other TMDs in their applications. Bearing this in mind, we expected ReS_2 not only to be an efficient photocatalyst but also to offer active sites as co-catalyst, which might provide new opportunities to photocatalytic H_2 evolution. Nevertheless, to the best of our knowledge, its potential as a co-catalyst for photocatalytic H_2 production has not been experimentally demonstrated yet, motivating to an in-depth study to shed light on new features of ReS_2.

In this work, ReS_2 has been successfully loaded on 1D CdS nanorods as co-catalysts via a facile two-step hydrothermal method (Scheme S1). 1D CdS nanorods provide a substrate for ReS_2 loading, and abundant catalytic sites and robust interaction between CdS and ReS_2 facilitate photogenerated electrons transfer, thus suppressing the recombination processes. As a result, CdS shows an enormously increased activity for hydrogen generation due to the presence of ReS_2 as co-catalyst. Importantly, the ReS_2/CdS composite loaded with 1 wt% ReS_2 exhibits the highest hydrogen production rate of 24.36 and 137.5 mmol h^{-1} g^{-1} using Na_2S-Na_2SO_3 and lactic acid as sacrificial reagents, respectively. With these rates, ReS_2/CdS far surpasses the rates of Pt/CdS and MoS_2/CdS under visible light irradiation.

2. Experimental section

2.1. Materials preparation

2.1.1. Synthesis of CdS NRs

In a typical synthesis of CdS NRs, 4.3 g $Cd(AC)_2{\cdot}2H_2O$ and 3.7 g thiourea were added to 30 ml of ethylenediamine in ultrasound, respectively. After dissolution, the ethylenediamine solution with thiourea was slowly added to the ethylenediamine solution with Cd $(AC)_2{\cdot}2H_2O$. The solution was transferred into a Teflon-lined autoclave and maintained at 160 °C for 24 h. After cooling to room temperature, CdS NRs was rinsed with distilled water and ethanol for several time, and dried in a vacuum oven at 60 °C overnight.

2.1.2. Synthesis of 1% ReS_2/CdS

10.02 mg NH_4ReO_4, 5.62 mg thioacetamide (C_2H_5NS) and 0.03 g hexamethylenetetramine was dissolved in 40 ml H_2O. After stirring for 15 min, a transparent solution was generated. Then, 400 mg CdS was immersed in the above solution. The solution was transferred into a Teflon-lined autoclave and maintained at 220 °C for 48 h. After cooling to room temperature, 1% ReS_2/CdS was rinsed with distilled water and ethanol for several time, and dried in a vacuum oven at 60 °C overnight.

2.2. Characterization

The phase and crystal structure of as-prepared samples were characterized by X-ray diffraction (XRD) on a Bruker D8 diffractometer using Cu Ka ($\lambda = 1.5406$) radiation in a 2θ range from 5° to 70°. Morphology and chemical composition of the samples were analyzed using the Sigma500 Zeiss Field emission scanning electron microscopy

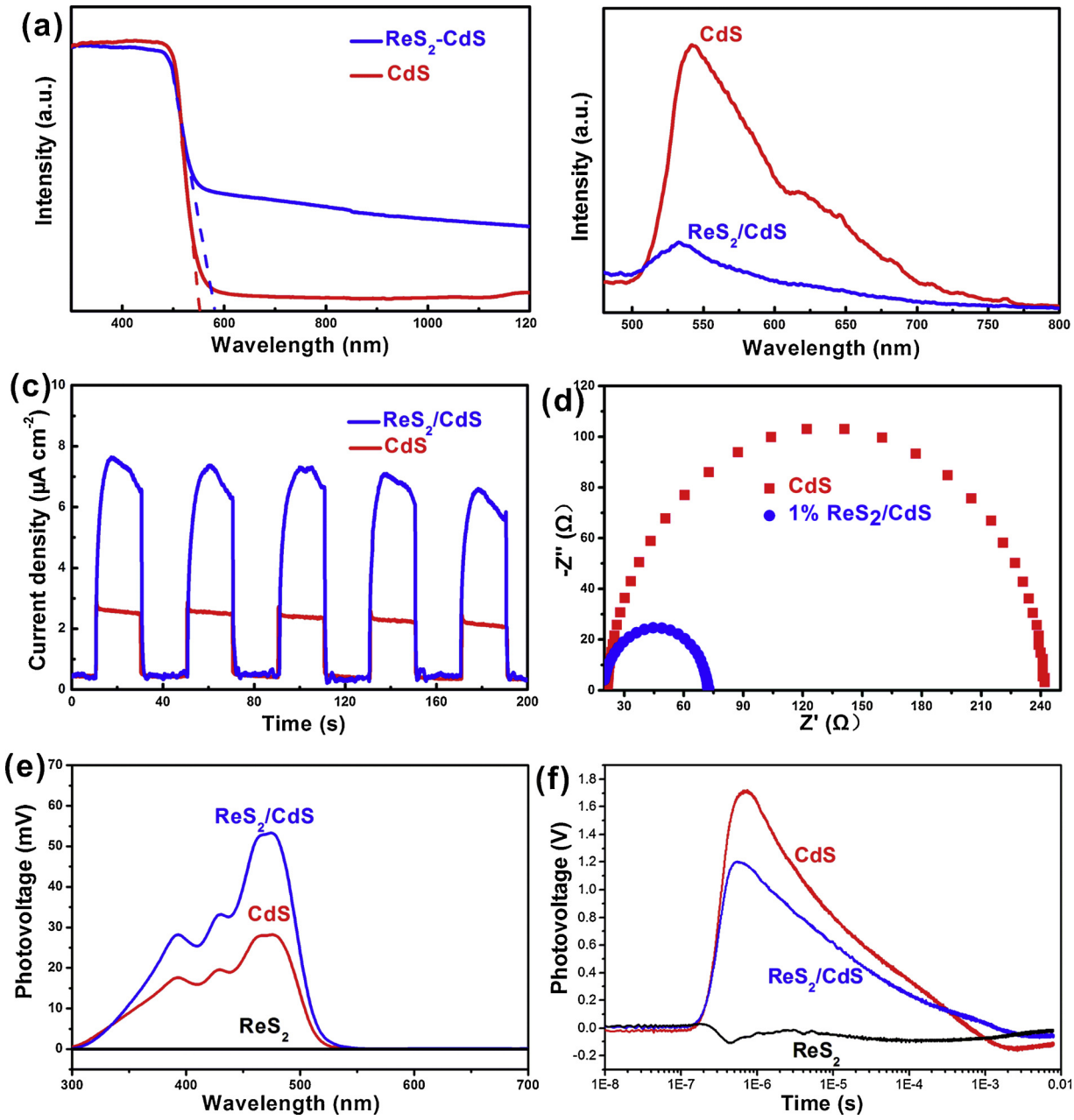

Fig. 2. Optical properties and charge carrier dynamics of ReS_2/CdS and CdS. (a) UV–Vis DRS spectra, (b) PL spectra, (c) photocurrent responses, (d) electrochemical impedance plots, (e) SPV spectra, and (f) TPV spectra.

(FESEM). The high-resolution transmission electron microscopy (HRTEM) images and element mapping were obtained by a JEO LJEM-2100 F (UHR) field emission transmission electron microscopy. X-ray photoelectron spectroscopy (XPS) data were obtained by Thermo ESCALAB 250XI X-ray photoelectron spectrometer (Al Ka, 150 W, C1s 284.8 eV). UV–vis diffuse reflectance spectroscopy (DRS) of samples were determined by a UV–vis spectrometer (Perkin Elmer, Lambda 850, $BaSO_4$ as a reference) and record on the within the scope of 200–800 nm. Time-resolved PL spectra (380 nm excitation) recorded by a FLS980 Multifunction Steady State and Transient State Fluorescence Spectrometer (Edinburgh Instruments, room temperature). The surface photovoltage spectra were measured by a TLS-SPV530 spectrometer (Zolix Instruments Co., Beijing). The transient surface photovoltage data were recorded by a 500 MHz digital oscilloscope (TDS 3054C, Tektronix, Beaverton, OR, USA). We placed the powder sample on the ITO electrode and another ITO electrode was used to press it to obtain a film composed of the powder sample. A laser pulse (λ = 355 nm with a pulse width of 4 ns) using the third-harmonic from a Nd:YAG laser (Quantel Brilliant Eazy: BRILEZ/IR-10) was employed as the light source. Inductively coupled plasma (ICP) spectrometer (Shimadzu, ICPE-9820) was used.

2.3. Photocatalytic H_2 production

The photocatalytic hydrogen tests were conducted in a Labsolar-III AG closed gas circulation and evacuation system (Beijing Perfect Light Technology Co., Ltd China) maintaining the photo-reaction temperature at 5 °C with a low-temperature thermostat bath (Poly Science, USA). In the photo-reaction system, 20 mg ReS_2/CdS was suspended in 50 ml of DI water containing 2.1 g Na_2S and 0.8 g Na_2SO_3 or 10% lactic acid as sacrifice reagent. A 300 W Xennon lamp (PLS-SXE-300UV, Beijing Trusttech Co. Ltd., China) with a UV-cutoff filter (providing

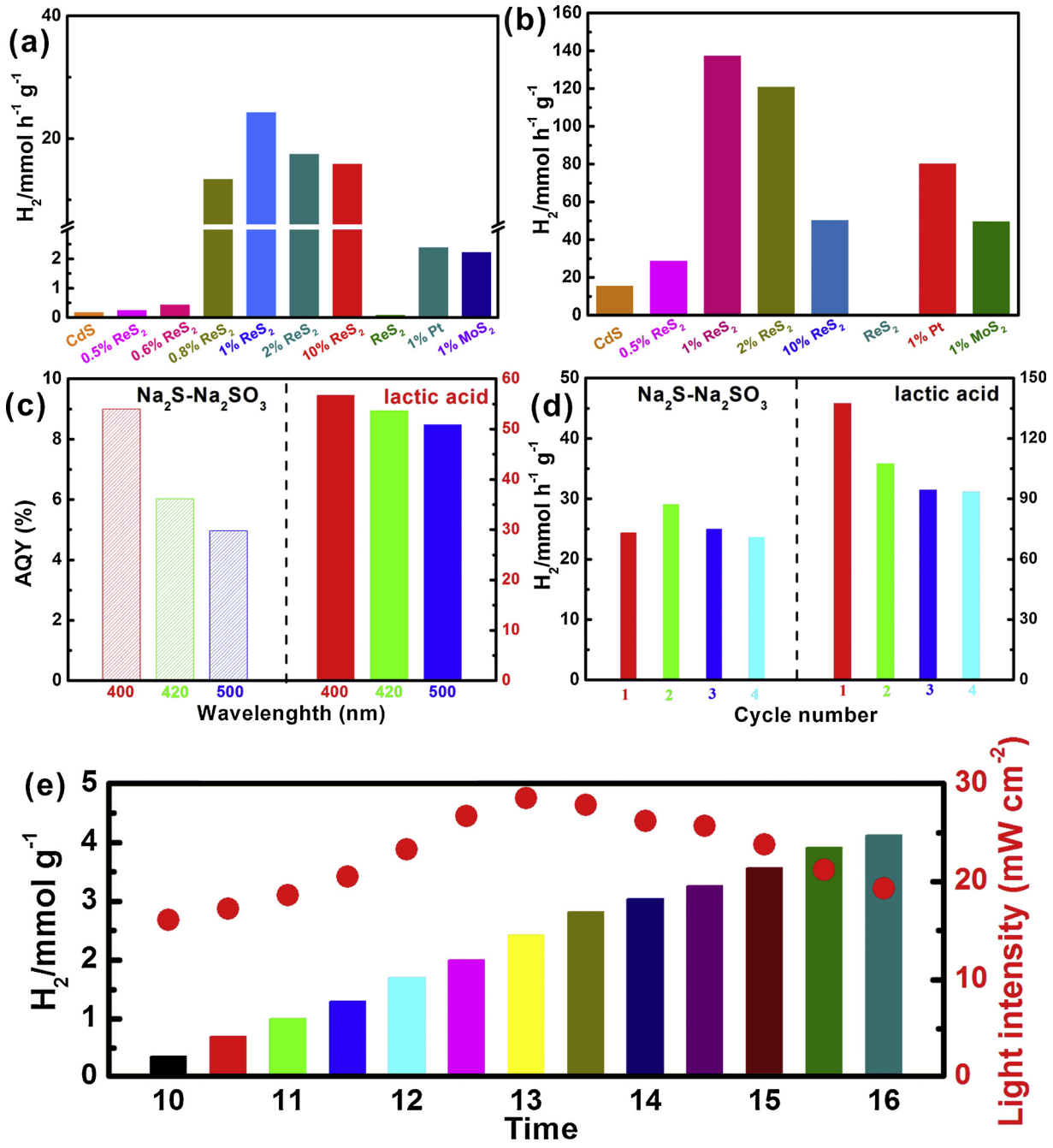

Fig. 3. Photocatalytic H_2 evolution on ReS_2/CdS and CdS photocatalysts. (a) Hydrogen generation rate of CdS with loading of ReS_2 at different amounts as well as other co-catalysts using Na_2S–Na_2SO_3 as sacrificial reagent under visible-light irradiation, (b) hydrogen generation rate of CdS with loading of ReS_2 at different amounts as well as other co-catalysts using lactic acid as sacrificial reagent under visible-light irradiation, (c) apparent quantum efficiency under irradiation with monochromatic light at different wavelengths, (d) recycling for hydrogen evolution of CdS with 1% ReS_2 loading, and (e) hydrogen generation of ReS_2/CdS under natural sunlight irradiation (from 10:00 to 16:00, 2018-6-6; 32°976′ N, 112°497′ E, Nanyang, China) in the feasibility study.

visible light $\lambda \geq 420$ nm) was served as the visible light source to trigger the water splitting reactions. To identify and quantify the gases produced, a volume of 1.5 ml of gas was hourly sampled and measured by a gas chromatography (GC9790II, Zhejiang Fuli Analytical Instrument Co., Ltd. China) equipped with a thermal conductivity detector (TCD) and a 5 Å molecular sieve column, where argon (Ar) was used as the carrier gas. The quantification of the H_2 yield were based on a calibration curve.

2.4. Apparent quantum efficiencies (AQE) calculations

The apparent quantum efficiency (AQE) was measured under the same photocatalytic reaction condition, except for the incident light wavelength. The H_2 yields of 1 h photoreaction under monochromatic light. AQE was calculated by the following equation:

$$\text{AQE} = \frac{N_{H2}}{N_p} = \frac{number\ of\ reacted\ electrons}{number\ of\ incident\ photons} \times 100\%$$

$$= \frac{2 \times the\ number\ of\ evolved\ H_2\ molecuies}{number\ of\ incident\ photons} \times 100\%$$

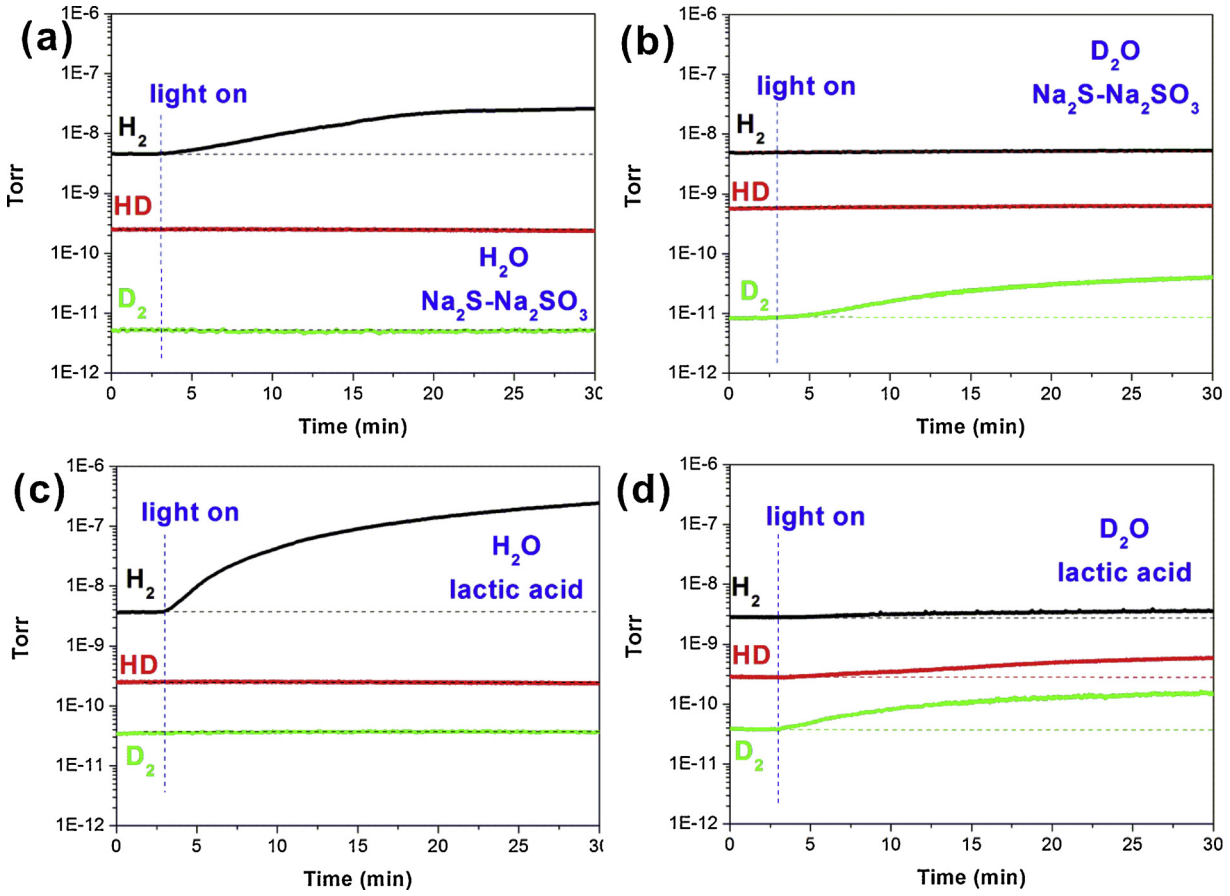

Fig. 4. On-line mass spectrometry of photocatalytic hydrogen production on ReS_2/CdS: (a) H_2O solution of Na_2S-Na_2SO_3; (b) D_2O solution of Na_2S-Na_2SO_3; (c) H_2O solution of lactic acid; and (d) D_2O solution of lactic acid.

2.5. Photoelectrochemical measurements

Photocurrent response and linear sweep voltammetry and electrochemical impedance of the catalysts were measured on an electrochemical workstation (CHI 630e) in a three-electrode quartz reactor using 0.5 M Na_2SO_4 solution and a mixed solution of 0.1 M $K_3[Fe(CN)_6]$ and $K_4[Fe(CN)_6]\cdot 3H_2O$, respectively, as the electrolyte solutions. Linear sweep voltammetry (LSV) is carried out at a scan rate of 10 mV/s from 0.4 to -0.6 V. Working electrodes for samples were prepared applying the doctor-blading method. Then, 0.01 g ethyl cellulose was dissolved in about 15 ml ethanol with 0.1 g catalyst. Subsequently, a glass stick was applied to FTO with a layer of high-temperature adhesive tape on the edge, followed by drying in air and activation at 120 °C for 2 h. All tests were done under visible light irradiation.

2.6. In-situ fourier transform infrared spectrometer (FT-IR) analysis

Fourier transform infrared spectrometer (Nicolet IS-50) was used for in-situ FT-IR measurement. The sample was filled into the in-situ IR cell, and Ar and H_2O gases were introduced into the cell and fibre source (FX300, Beijing Perfect light Technology Co., Ltd China) through the CaF_2 window of the cell. Before the measurement, the sample was degassed at 423 K for 4 h. The baseline was obtained after adsorption equilibrium on the sample for 1 h. 1%ReS_2/CdS was used after treatment by Na_2S-Na_2SO_3 or lactic acid solution.

2.7. On-line mass spectrometry analysis

10 mg photocatalyst, 2.1 g–0.8 g Na_2S-Na_2SO_3 in 10 ml H_2O/D_2O or 10% lactic acid solution were added to the closed quartz reactor (Beijing Perfect light Technology Co., Ltd., China). One end of the reactor is continuously fed into Ar and the other end is fed into the mass spectrometry (HPR-20 R&D, Beijing Hiden Analytical Technology Co., Ltd., China) sampling port. Using SEM detector, H_2 and D_2 were detected simultaneously in MID mode. After the MS baseline is stable, 300 W high pressure xenon lamp (PLS-SXE300, Beijing Perfect light Technology Co., Ltd., China) is used to illuminate the gas products in the reactor on-line.

2.8. Computational details

Density functional theory (DFT) calculations were performed using DMol^3 procedure based on Materials Studio software. The electron exchange and correlation were approximated by generalized gradient approximation (GGA) with the Perdew-Burke-Ernzerhof (PBE) functional. Dispersion correction by Grimme (DFT-D) was used to describe the van der Waals interaction. The valence electron configurations were $1s^1$ for H, $4f^{14}5d^56s^2$ for Re, $4d^55s^1$ for Mo and $3s^23p^4$ for S, respectively. As for the Monkhorst-Pack grid *k*-point in the Brillouin-zone, a $5 \times 5 \times 1$ *k*-point was used for geometry optimizations. For convergence threshold, the total energy of the system, maxforce, and displacement tolerances were set to be $1 \times 10^{-}5$Ha, 0.02 Ha/Å, and 0.05 Å, respectively.

The rhenium disulphide (ReS_2) and molybdenum disulphide (MoS_2) were constructed via the slab mode along the (100) and (001) orientation, respectively. The surface of ReS_2 and MoS_2 in order to match the numbers of atoms were constructed to be 2×2 and 4×4, respectively. In order to avoid interaction of two slab a vacuum space of 15 Å was built.

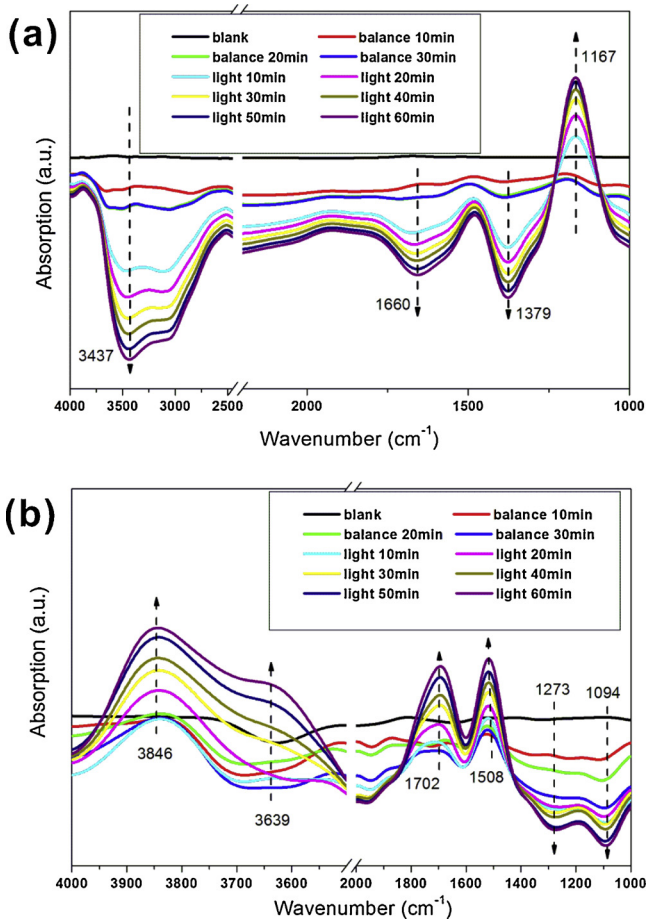

Fig. 5. *In situ* FT-IR spectra of the H_2O reaction on ReS_2/CdS with (a) Na_2S-Na_2SO_3 and (b) lactic acid as sacrificial reagent.

3. Results and discussions

Structures and compositions of ReS_2/CdS (1 wt% of ReS_2) are visualized in Fig. 1. All peaks in the X-ray powder diffraction (XRD) pattern of ReS_2/CdS can be indexed to be hexagonal CdS phase (JCPDS No. 41-1049), and no peaks related to ReS_2 are observed, which may be due to its low content and crystallization degree (Figs. 1a and S1) [30]. Pure CdS exhibits nanorod morphology (ca. 200–400 nm in length and 40–50 nm in diameter), while ReS_2 forms nanoparticles (ca. 200 nm in diameter; Figs. S2, S3). ReS_2 loading onto CdS did not significantly alter the nanorod morphology of CdS, and obvious interfaces form between ReS_2 and CdS, indicating that ReS_2 is tightly bound to the CdS nanorod surface. This finding was revealed by scanning electron microscopy (SEM) and transmission electron microscopy (TEM) of ReS_2/CdS (Fig. 1b–d). Furthermore, the structural characteristics of two selected ReS_2 and CdS substrates were detected by high-resolution TEM (HRTEM) (Fig. 1e–g). For CdS, an interplanar distance of 0.336 nm indexed to the (001) lattice plane is observed, and the fast Fourier-transform (FFT)-filtered image reveals a high degree of crystallinity (Fig. 1h). For ReS_2, there are no obvious lattice fringes, which indicated that ReS_2 was non-crystalline. Energy dispersive X-ray spectroscopy (EDS) spectra (Fig. S4) confirm the existence of the elements Cd, S, and Re. Element mapping of ReS_2/CdS corresponding to the area marked in Fig. 1i is shown in Fig. 1j–l, confirming that elemental S is uniformly dispersed in the whole selected area, while Re and Cd are distributed separately, indicating an intimate contact between ReS_2 and CdS. Effective interfacial contact shortens the charge transfer distance and, thus, facilitates the electron transfer between CdS and ReS_2. In addition, XPS and inductively coupled plasma (ICP) shows a ReS_2 content of about 0.8 wt%. According to the Pauling scale, Re has a higher electronegativity than Cd (1.9 *vs* 1.69), implying that electrons are transferred from CdS to ReS_2 at their interface in the ReS_2/CdS nanocomposite [31]. This result is confirmed by the higher Cd binding energy in ReS_2 (1 wt%)/CdS than in pure CdS, indicating a decrease of the electron density of Cd after ReS_2 loading (Fig. S5). To further characterize surface chemical composition and valence state, ReS_2/CdS was analyzed by X-ray photoelectron spectroscopy (XPS). As shown in Fig. 1m, n, the Cd 1 s and S 2p XPS spectra exemplarily demonstrate the structural characteristics of CdS [32]. Fig. 1o shows two distinct peaks at 41.8 and 44.2 eV, which can be assigned to the Re 4f 7/2 and Re 4f 5/2 states of Re^{4+} in ReS_2, respectively [33]. All the above results corroborate the successful deposition of ReS_2 on the CdS nanorod surface.

The effect of ReS_2 modification on the optical properties of CdS was studied by UV–Vis diffusion reflection spectroscopy (Fig. 2a). ReS_2 loading on CdS apparently enhances the light absorption across the whole visible light region for ReS_2/CdS with respect to pure CdS. This may be ascribed to the intrinsically high visible light harvesting ability of black-colored ReS_2 nanoparticles (Fig. S6). Moreover, the absorption edge of ReS_2/CdS shows a distinct red shift, implying that ReS_2 loading reduces the intrinsic band gap of CdS. According to the plot of $(ahv)^2$ versus energy (hv), the band gaps (Eg) of ReS_2/CdS and CdS were calculated as 2.02 eV and 2.20 eV, respectively (Fig. S7) [34]. To corroborate the underlying alteration of the band structure, VB and CB positions of ReS_2/CdS and CdS were determined from the XPS valence band spectrum (Fig. S8) and Mott-Schottky plots (Fig. S9), respectively. We found that the CB position becomes more negative after the introduction of ReS_2 (Fig. S10), which facilitates the reduction reaction.

To further understand the impact of the ReS_2 co-catalyst on the charge separation, photoluminescence (PL) spectra, luminescent decay, and photo-electrochemical measurements were carried out. In the PL spectra (Fig. 2b), the intensities of the ReS_2/CdS peaks are much weaker, implying that ReS_2 loading largely suppresses the recombination of electron–hole pairs [35,36]. To confirm and better understand the enhanced migration and separation of photo-induced charge carriers of ReS_2/CdS, photoelectrochemical measurements were recorded. As expected, ReS_2/CdS shows a nearly 2.5 times higher photocurrent intensity than bare CdS, which infers that ReS_2 is an effective co-catalyst to promote the migration of photo-induced carriers (Fig. 2c) [37,38]. Meanwhile, the effect of ReS_2 deposition on the kinetics of charge migration is further studied by electrochemical impedance spectroscopy (EIS) [32]. In comparison with pure CdS, the semicircle in the Nyquist plot of ReS_2/CdS has a smaller radius, indicative of an accelerated charge transport and improved charge separation during photocatalysis, which demonstrates the prominent role of ReS_2 nanoparticles loaded on CDs as co-catalysts (Fig. 2d) [37,38]. Linear-sweep-voltammetry (LSV) of ReS_2/CdS and MoS_2/CdS was performed in 0.5 M $NaSO_4$ solution using a typical three-electrode cell under visible light irradiation (Fig. S11). The current intensity of MoS_2/CdS at negative voltage region is lower than that of ReS_2/CdS, suggesting that generation, transfer, and separation of photo-induced electrons and holes is more efficiently facilitated by ReS_2 than MoS_2 loaded on CdS [39,40]. Therefore, ReS_2/CdS has a better photocatalytic performance than MoS_2/CdS, which is consistent with the above conclusions.

On the other hand, the transport behavior of photo-induced carriers was analyzed from surface photovoltage (SPV) and transient photovoltage (TPV) spectra [41,42]. The SPV signal results from the change of the surface potential after light irradiation. Higher intensities indicate effective separation of photo-induced carriers. Therefore, this method is a very effective way to study the effect of the co-catalyst on the transport of photo-induced carriers on semiconductor photocatalysts. As shown in Fig. 2e, ReS_2 did not exhibit an obvious SPV response. However, CdS and ReS_2/CdS showed the same peak type and displayed a positive SPV response between 300–530 nm, but ReS_2/CdS showed a higher intensity than CdS. This indicates that CdS is an n-type photocatalyst, and photo-induced electrons migrate to the bulk. After

ReS_2 loading on the CdS surface, the separation of photo-induced charge carriers was enhanced by ReS_2 acting as electron acceptor [41,42]. TPV spectra (Fig. 2f) also allowed some similar conclusions as SPV. (1) CdS and ReS_2/CdS were positive, indicating the accumulation of positive charge near the surface. However, the TPV signal of ReS_2 was negative charged [41,42]. (2) An obvious retardation is observed in the TPV spectrum of ReS_2/CdS in comparison with that of bare CdS at longer times than 2.8×10^{-4} s. Hence, the interface between CdS and ReS_2 possibly reduces the transfer rate and inhibits the recombination of photo-induced charge carriers [41,42].

Owing to the unique characteristics of ReS_2 to promote light absorption and charge separation, we examined the role of ReS_2 as co-catalyst loaded on CdS in photocatalytic hydrogen production. Fig. 3a shows the hydrogen production over ReS_2/CdS photocatalysts with different ReS_2 contents in the presence of Na_2S–Na_2SO_3 (pH = 12.8) as sacrificial electron donor under visible light irradiation. Pure CdS and ReS_2 showed a relatively low photocatalytic activity (0.192 mmol $h^{-1} g^{-1}$ for CdS and 0.102 mmol $h^{-1} g^{-1}$ for ReS_2). After loading a small amount of ReS_2 (0.5 wt%), the hydrogen evolution rate of ReS_2/CdS increased compared with that of pure CdS to a value of 0.263 mmol $h^{-1} g^{-1}$. The highest hydrogen generation activity of 24.357 mmol $h^{-1} g^{-1}$ was achieved for a ReS_2 loading of 1 wt%, which is about 127 times higher than the generation activity of pure CdS. However, a further increase in ReS_2 loading decreases the hydrogen evolution activity due to the decreased carrier separation efficiency,[23,24] but this activity is still much higher than that of pure CdS and ReS_2. Moreover, ReS_2/CdS has even a higher photocatalytic hydrogen generation activity than MoS_2(1 wt%)/CdS and Pt (1 wt%/CdS under the same conditions, showing that noble-metal-free ReS_2 possibly presents an alternative co-catalyst for replacing the noble metal Pt and is an even better co-catalyst than MoS_2. In order to confirm the enhancing effect of ReS_2, we studied the H_2 production over all photocatalysts using lactic acid (pH = 1.5) as sacrificial electron donor, as shown in Fig. 3b. Under visible light irradiation, CdS(1 wt%)/ReS_2 still exhibits the highest photocatalytic hydrogen evolution rate of 137.5 mmol $h^{-1} g^{-1}$, which is 8.8 and 2.8 fold larger than those of bare CdS and MoS_2/CdS, respectively. This indicates that ReS_2 can be used as co-catalyst in a wide pH range from acidic to basic pH.

To understand the enhanced photocatalytic hydrogen evolution in detail, the apparent quantum efficiency (AQY) of ReS_2(1 wt%)/CdS was calculated at different irradiation wavelengths, as shown in Fig. 3c. The AQYs of the Na_2S-Na_2SO_3 system are 9.03%, 6.02%, and 4.06% at wavelengths of 400, 420, and 500 nm, respectively. In contrast, the lactic acid system showed higher AQYs of 56.76%, 53.64%, and 50.88% at 400, 420, and 500 nm, respectively. When compared with MoS_2-modified CdS, ReS_2(1 wt%)/CdS showed the best hydrogen yield rate and AQY (Table S1). The above results demonstrate that ReS_2 is a very promising candidate as co-catalyst for hydrogen evolution. Additionally, to verify the importance of an intimate contact between ReS_2 and CdS during the photocatalytic process, we studied the photocatalytic process on a physical mixture of ReS_2 and CdS nanorods (1 wt % of ReS_2 *vs* CdS), which showed a very poor hydrogen evolution amount of 0.203 mmol $h^{-1} g^{-1}$. Comparison with the photocatalytic process on ReS_2 (1 wt%)/CdS proves that the hydrogen evolution performance over ReS_2/CdS is greatly influenced by the effective interaction between CdS and ReS_2 species. At present, CdS-based materials present the most effective photocatalysts for photocatalytic hydrogen evolution. Therefore, we investigated the feasibility of using natural sunlight irradiation for industrial hydrogen production with solar energy. As shown in Fig. 3e, ReS_2 (1 wt%)/CdS displayed high hydrogen production (4.12 mmol g^{-1}) in the presence of Na_2S–Na_2SO_3 as sacrificial electron donor after 6 h sunlight irradiation. This hydrogen production exceeds the H_2 evolution on CdS (1.02 mmol g^{-1}) and g-C_3N_4 (0.04 mmol g^{-1}) under Xenon lamp irradiation (laboratory conditions), which implies that ReS_2/CdS can be used as industrial photocatalyst for hydrogen evolution using natural solar energy irradiation.

To comprehensively elucidate the photocatalytic hydrogen evolution over ReS_2/CdS at the molecular level, theoretical calculations, online mass spectrometry, and *in situ* Fourier transform infrared spectroscopy (FT-IR) were performed. As shown in Fig. S12, H_2O activation on the surfaces of ReS_2 and MoS_2 was also compared based on theoretical DFT calculations. The bond angle of the water molecule on ReS_2 is 103.685°, while it is 103.568° on (001) MoS_2, demonstrating that ReS_2 possesses a strong ability to polarize water molecules. Therefore, ReS_2 is a better co-catalyst for photocatalytic H_2 production than MoS_2.

In the field of photocatalytic hydrogen production, sacrifice reagents are often used to improve the hydrogen production activity, but these reagents may also be hydrogen sources. To determine that water is indeed decomposed to hydrogen, isotope experiments were performed. When Na_2S-Na_2SO_3 was used as sacrificial reagent in H_2O solution, only H_2 was found and neither HD nor D_2 was detected (Fig. 4a). In D_2O solution, only D_2 and no H_2 or HD was detected (Fig. 4b). This proves that all hydrogen gas is derived from water, and Na_2S-Na_2SO_3 only acts as deoxidizer to consume photo-generated holes. But, using lactic acid as sacrificial reagent gave different results. In H_2O solution of lactic acid, only H_2 was found and neither HD nor D_2 was detected (Fig. 4c). However, in D_2O solution of lactic acid, all H_2, HD, and D_2 species were detected (Fig. 4d). This proves that lactic acid can also be decomposed to hydrogen. Furthermore, HD generation implies that the interaction between lactic acid and water improves the hydrogen production. The total amount of produced hydrogen (H_2, HD, and D_2) is almost the same for both H_2O and D_2O solutions, indicating that D_2O does not affect the hydrogen generation activity. In addition, the amount of produced hydrogen for lactic acid solution is higher than that for Na_2S-Na_2SO_3 solution, which is in agreement with the above photocatalytic results (Fig. 3). More importantly, we found that the amount of D atoms produced in the lactic acid system is similar to that produced in the Na_2S-Na_2SO_3 system (Fig. 4b,d). This suggests that the photocatalytic ability for water splitting is the same in different sacrifice reagents. The higher hydrogen amount of the lactic acid system is attributed to the extra hydrogen atoms of lactic acid.

Fig. 5 shows the *in situ* FT-IR spectra of the H_2O reaction on ReS_2/CdS. For Na_2S-Na_2SO_3 as sacrificial reagent (Fig. 5a), the spectrum shows a peak at 3437 cm^{-1} that can be attributed to the stretching vibration of adsorbed H_2O molecules. The two peaks at 1660 and 1379 cm^{-1} can be assigned to the stretching vibration of adsorbed SO_3^{2-} [43–46]. The peak at 1167 cm^{-1} can be assigned to the stretching vibration of SO_4^{2-}. After illumination for 60 min, IR peaks of H_2O and SO_3^{2-} decreased with no obvious position change. On the contrary, IR peaks of SO_4^{2-} increased with increasing light illumination. This result indicates that H_2O splits during the photocatalytic hydrogen evolution, and that SO_3^{2-} as sacrificial reagent also oxidizes to SO_4^{2-}. For lactic acid as sacrificial reagent (Fig. 5b), the two peaks at 1094 and 1273 cm^{-1} can be assigned to the stretching vibrations of C—O and O—H in alcohol groups [47,48]. The two peaks at 1508 and 1702 cm^{-1} can be attributed to the stretching vibration of carboxyl groups, [47,48] and the two peaks at 3639 and 3847 cm^{-1} can be assigned to the stretching vibrations of surface hydroxyl group [47]. After illumination for 60 min, the IR peaks of the alcohol groups decreased with no obvious position change. On the contrary, the IR peaks of carboxyl groups and surface hydroxyl groups increased with the increasing illumination time. This result indicates that lactic acid decomposed into −OH and −COOH groups, which reacted with water to hydrogen.

Experimental evidence, including ultrafast spectroscopy, electrochemical testing, *in situ* FT-IR, and on-line mass spectrometry, as well as theoretical calculations indicates that photocatalytic hydrogen evolution over ReS_2/CdS occurs according to the process illustrated in **Scheme S2**. Under visible light irradiation, the photo-generated electrons of CdS migrate to ReS_2, which acts as an electron collector, inhibiting charge recombination and accelerating the activation of molecular H_2O to enhance the photocatalytic production of hydrogen.

Na_2S-Na_2SO_3 and lactic acid react with photo-generated holes to inhibit charge recombination and accelerate the generation of intermediate products, enhancing the photocatalytic hydrogen production.

4. Conclusions

In summary, we successfully developed ReS_2 as a highly efficient co-catalyst on CdS nanorods for extraordinarily efficient photocatalytic hydrogen evolution. The optimal photocatalytic hydrogen evolution rate of ReS_2/CdS is 137.5 mmol h^{-1} g^{-1}, and the quantum efficiency at 420 nm is 53.64%. More importantly, ReS_2/CdS can be used as industrial photocatalyst for hydrogen evolution using natural solar energy. The excellent catalytic activity is attributed to the fast charge separation and excellent activation of water due to the robust interaction between CdS and ReS_2. In addition, photocatalytic hydrogen evolution over ReS_2/CdS was comprehensively elucidated at the molecular level using theoretical calculations, on-line mass spectrometry, and *in situ* FT-IR. It is anticipated that this work promotes the development of hydrogen production systems with advanced co-catalyst providing extremely high photocatalytic activities.

Acknowledgments

This work was supported by the National Natural Science Foundation of China (Nos. 51872147, 21671113), the 111 Project of Hubei Province (2018-19-1), the Program for Innovative Research Team of Science and Technology in the University of Henan Province (19IRTSTHN025) and supported by Open Fund (PEBM201702) of Key Laboratory for Photonic and Electric Bandgap Materials, Ministry of Education (Harbin Normal University).

Appendix A. Supplementary data

Supplementary material related to this article can be found, in the online version, at doi:https://doi.org/10.1016/j.apcatb.2019.117897.

References

[1] H. Kisch, Semiconductor photocatalysis mechanistic and synthetic aspects, Angew. Chem. Int. Ed. 52 (2013) 812–847.
[2] J. Li, X. Gao, B. Liu, Q. Feng, X.B. Li, M.Y. Huang, Z. Liu, J. Zhang, C.H. Tung, L.Z. Wu, Graphdiyne: a metal-free material as hole transfer layer to fabricate quantum dot-sensitized photocathodes for hydrogen production, J. Am. Chem. Soc. 138 (2016) 3954–3957.
[3] X. Wang, K. Maeda, A. Thomas, K. Takanabe, G. Xin, J.M. Carlsson, K. Domen, M. Antonietti, A metal-free polymeric photocatalyst for hydrogen production from water under visible light, Nat. Mater. 8 (2009) 76–80.
[4] L. Cheng, Q. Xiang, Y. Liao, H. Zhang, CdS-based photocatalysts, Energy Environ. Sci. 11 (2018) 1362–1391.
[5] Y.J. Yuan, Z.T. Yu, D.Q. Chen, Z.G. Zou, Metal-complex chromophores for solar hydrogen generation, Chem. Soc. Rev. 46 (2017) 603–631.
[6] L. Jing, W. Zhou, G. Tian, H. Fu, Surface tuning for oxide-based nanomaterials as efficient photocatalysts, Chem. Soc. Rev. 42 (2013) 9509–9549.
[7] Z.R. Tang, B. Han, C. Han, Y.J. Xu, One dimensional CdS based materials for artificial photoredox reactions, J. Mater. Chem. A 5 (2017) 2387–2410.
[8] A. Nag, S. Sapra, C. Nagamani, A. Sharma, N. Pradhan, S.V. Bhat, D.D. Sarma, A study of Mn^{2+} doping in CdS nanocrystals, Chem. Mater. 19 (2007) 3252–3259.
[9] N.J. Borys, M.J. Walter, J. Huang, D.V. Talapin, J.M. Lupton, The role of particle morphology in interfacial energy transfer in CdSe/CdS heterostructure nanocrystals, Science. 330 (2010) 1371–1374.
[10] J. Yang, H. Yan, X. Wang, F. Wen, Z. Wang, D. Fan, J. Shi, C. Li, Roles of cocatalysts in Pt-PdS/CdS with exceptionally high quantum efficiency for photocatalytic hydrogen production, J. Catal. 290 (2012) 151–157.
[11] J. Yang, D. Wang, H. Han, C. Li, Roles of cocatalysts in photocatalysis and photoelectrocatalysis, Accounts. Chem. Res. 46 (2013) 1900–1909.
[12] J. Ran, J. Zhang, J. Yu, M. Jaroniec, S.Z. Qiao, Earth-abundant cocatalysts for semiconductor-based photocatalytic water splitting, Chem. Soc. Rev. 43 (2014) 7787–7812.
[13] L. Zhang, X. Fu, S. Meng, X. Jiang, J. Wang, S. Chen, Ultra-low content of Pt modified CdS nanorods: one-pot synthesis and high photocatalytic activity for H2 production under visible light, J. Mater. Chem. A 3 (2015) 23732–23742.
[14] Y.J. Zhang, L. Zhang, Preparation of Ru-Loaded CdS/Al-HMS nanocomposites and production of hydrogen by photocatalytic degradation of formic acid, Appl. Surf. Sci. 255 (2009) 4863–4866.
[15] W. Yao, C. Huang, N. Muradov, T. Ali, A novel Pd–Cr_2O_3/CdS photocatalyst for solar hydrogen production using a regenerable sacrificial donor, Int. J. Hydrogen Energy 36 (2011) 4710–4715.
[16] X. Zhang, Y. Li, J. Zhao, S. Wang, Y. Li, H. Dai, X. Sun, Advanced three-component ZnO/Ag/CdS nanocomposite photoanode for photocatalytic water splitting, J. Power Sources 269 (2014) 466–472.
[17] H. Tada, T. Mitsui, T. Kiyonaga, T. Akita, K. Tanaka, All-solid-State Z-Scheme in CdS-Au-TiO_2 three-component nanojunction system, Nat. Mater. 5 (2006) 782.
[18] L. Kong, Y. Dong, P. Jiang, G. Wang, H. Zhang, Na. Zhao, Light-assisted rapid preparation of a Ni/g-C_3N_4 magnetic composite for robust photocatalytic H_2 evolution from water, J. Mater. Chem. A 4 (2016) 9998–10007.
[19] X. Yue, S. Yi, R. Wang, Z. Zhang, S. Qiu, Cadmium sulfide and nickel synergetic Co-catalysts supported on graphitic carbon nitride for visible-light-Driven photocatalytic hydrogen evolution, Sci. Rep. 6 (2016) 22268.
[20] Z. Sun, H. Zheng, J. Li, P. Du, Extraordinarily efficient photocatalytic hydrogen evolution in water using semiconductor nanorods integrated with crystalline Ni_2P cocatalysts, Energy Environ. Sci. 8 (2015) 2668–2676.
[21] M. Liu, Y. Chen, J. Su, J. Shi, X. Wang, L. Guo, Photocatalytic hydrogen production using twinned nanocrystals and an unanchored NiS_x co-catalyst, Nat. Energy. 1 (2016) 16151.
[22] X. Chen, W. Chen, H. Gao, Y. Yang, W. Shangguan, In situ photodeposition of NiO_x on CdS for hydrogen production under visible light: enhanced activity by controlling solution environment, Appl. Catal. B: Environ. 152 (2014) 68–72.
[23] X. Zong, H. Yan, G. Wu, G. Ma, F. Wen, L. Wang, C. Li, Enhancement of photocatalytic H_2 evolution on CdS by loading MoS_2 as cocatalyst under visible light irradiation, J. Am. Chem. Soc. 130 (2008) 7176–7177.
[24] K. Chang, X. Hai, J. Ye, Transition metal disulfides as noble-metal-Alternative Co-catalysts for solar hydrogen production, Adv. Energy Mater. 6 (2016) 1502555.
[25] Q. Zhang, W. Wang, J. Zhang, X. Zhu, Q. Zhang, Z. Zhang Ren, S. Song, J. Wang, Z. Ying, R. Wang, X. Qiu, T. Peng, L. Fu, Highly efficient photocatalytic hydrogen evolution by ReS_2 via a two-electron catalytic reaction, Adv. Mater. 30 (2018) 1707123.
[26] Q. Zhang, W. Wang, J. Zhang, X. Zhu, L. Fu, Thermally induced bending of ReS_2 nanowalls, Adv. Mater. 30 (3) (2018) 1704585.
[27] H. Liu, B. Xu, J.M. Liu, J. Yin, F. Miao, C.G. Duan, X.G. Wan, Highly efficient and ultrastable visible-light photocatalytic water splitting over ReS_2, Phys. Chem. Chem. Phys. 18 (21) (2016) 14222–14227.
[28] Q. Zhang, S. Tan, R.G. Mendes, Z. Sun, Y. Chen, X. Kong, Y. Xue, M.H. Rümmeli, X. Wu, S. Chen, L. Fu, Extremely weak van der waals coupling in vertical ReS_2 nanowalls for high-current-Density lithium-ion batteries, Adv. Mater. 28 (2016) 2616–2623.
[29] M. Mao, C. Cui, M. Wu, M. Zhang, T. Gao, X. Fan, J. Chen, T. Wang, J. Ma, C. Wang, Flexible ReS_2 Nanosheets/N-doped carbon nanofibers-based paper as a universal anode for alkali (Li, Na, K) ion battery, Nano Energy 45 (2018) 346–352.
[30] J.S. Jang, U.A. Joshi, J.S. Lee, Solvothermal synthesis of CdS nanowires for photocatalytic hydrogen and electricity production, J. Phys. Chem. C. 111 (2007) 13280–13287.
[31] H. Wang, S.B. Naghadeh, C. Li, L. Ying, A. Allen, J.Z. Zhang, Enhanced photoelectrochemical and photocatalytic activities of CdS nanowires by surface modification with MoS_2 nanosheets, Sci. China Mat. 61 (6) (2018) 839–850.
[32] Yan Z., Yu X., Zhang Y., Jia H., Sun Z., Du P. Enhanced Visible Light-Driven Hydrogen Production from Water by a Noble-Metal-Free System Containing Organic Dye-Sensitized Titanium Dioxide Loaded with Nickel Hydroxide as the Cocatalyst, Appl. Catal. B: Environ. 160, 173–178.
[33] Corbet C. M., McClellan C., Rai A., Sonde S. S., Tutuc E., Banerjee S. K. Field Effect Transistors with Current Saturation and Voltage Gain in Ultrathin ReS2, ACS nano. 9, 363–370.
[34] Han Z., Chen G., Li C., Yu Y., Zhou Y. Preparation of 1D Cubic Cd0.8Zn0.2S Solid-Solution Nanowires Using Levelling Effect of TGA and Improved Photocatalytic H2-Production Activity, J. Mater. Chem. A. 3, 1696–1702.
[35] L. Ye, X. Jin, C. Liu, C. Ding, H. Xie, K.H. Chu, P.K. Wong, Thickness-ultrathin and bismuth-rich strategies for BiOBr to enhance photoreduction of CO_2 into solar fuels, Appl. Catal. B: Environ. 187 (2016) 281–290.
[36] Z. Ma, P. Li, L. Ye, Y. Zhou, F. Su, C. Ding, H. Xie, Y. Bai, P.K. Wong, Oxygen vacancies induced exciton dissociation of flexible BiOCl nanosheets for effective photocatalytic CO_2 conversion, J. Mater. Chem. 5 (2017) 24995–25004.
[37] L. Ye, C. Han, Z. Ma, Y. Leng, J. Li, X. Ji, D. Bi, H. Xie, Z. Huang, Ni_2P Loading on $Cd_{0.5}Zn_{0.5}S$ Solid Solution for Exceptional Photocatalytic Nitrogen Fixation Under Visible Light, Chem. Eng. J. 307 (2017) 311–318.
[38] Y. Bai, L. Ye, L. Wang, X. Shi, P. Wang, W. Bai, P.K. Wong, G-C_3N_4/$Bi_4O_5I_2$ heterojunction with I_3^-/I^- redox mediator for enhanced photocatalytic CO_2 conversion, Appl. Catal. B: Environ. 194 (2016) 98–104.
[39] F. Ning, M. Shao, S. Xu, Y. Fu, R. Zhang, M. Wei, D.G. Evans, X. Duan, TiO2/graphene/NiFe-layered double hydroxide nanorod array photoanodes for efficient photoelectrochemical water splitting, Energy Environ. Sci. 9 (2016) 2633–2643.
[40] Q. Yu, X. Meng, T. Wang, P. Li, J. Ye, Hematite films decorated with nanostructured Ferric Oxyhydroxide as photoanodes for efficient and stable photoelectrochemical water splitting, Adv. Funct. Mater. 25 (18) (2015) 2686–2692.
[41] F. Zhao, L.Q. Shi, J.B. Cui, Y.H. Lin, Photogenerated charge-transfer properties of Au-Loaded ZnO hollow sphere composite materials with enhanced photocatalytic activity, Acta Phys. -Chim. Sin. 32 (8) (2016) 2069–2076.
[42] W. Fa, P. Wang, B. Yue, F. Yang, D. Li, Z. Zheng, Ag_3PO_4/Ag_2CO_3 p–n heterojunction composites with enhanced photocatalytic activity under visible light, Chin. J. Catal. 36 (2015) 2186–2193.
[43] F. Li, Q. Gu, Y. Niu, R. Wang, Y. Tong, S. Zhu, H. Zhang, Z. Zhang, X. Wang, Hydrogen evolution from aqueous-phase photocatalytic reforming of ethylene

glycol over Pt/TiO_2 catalysts: Role of Pt and product distribution, Appl. Sur. Sci. 391 (2017) 251–258.
[44] H.A. Al-Abadleh, V.H. Grassian, FT-IR study of water adsorption on aluminum oxide surfaces, Langmuir 19 (2003) 341–347.
[45] E. Yoda, FT-IR study of dissociative water adsorption on 1-Butyl-3-methylimidazolium exchanged mordenite zeolite, J. Phys. Chem. C 113 (2009) 9851–9856.
[46] L. Li, R. Bennett, W. Conway, H. Yu, S. Clifford, M. Maeder, G. Puxty, Development and evaluation of a novel method for determining absorbent composition in aqueous ammonia-based CO_2 and SO_3^{2-} and SO_4^{2-} loaded capture process solutions via FT-IR spectroscopy, Energy Fuels 32 (2018) 8563–8570.
[47] Y.K. Chen, Y.F. Lin, Z.W. Peng, J.L. Lin, Transmission FT-IR study on the adsorption and reactions of lactic acid and poly (lactic acid) on TiO_2, J. Phys. Chem. C. 114 (2010) 17720–17727.
[48] T. Ube, Y. Yoneyama, T. Ishiguro, *In situ* Measurement of the pH-dependent Transmission Infrared Spectra of Aqueous Lactic Acid Solutions, Anal. Sci. 33 (2017) 1395–1400.